ELSEVIER

Catalysis Today 81 (2003) 263–286

CATALYSIS TODAY

www.elsevier.com/locate/cattod

The structure–activity relationships of methane mono-oxygenase mimics in alkane activation

Peter-Paul H.J.M. Knops-Gerrits [a,*], William A. Goddard III [b,1]

[a] *Département de Chimie, Université Catholique de Louvain (UCL), CMAT, Place L. Pasteur no. 1, B-1348 Louvain-la-Neuve, Belgium*
[b] *Material & Process Simulation Center, Beckman Institute (139-74), California Institute of Technology, Pasadena, CA 91125, USA*

Abstract

Activation of non reactive C–H bonds and their transformation into C–OH alcohol groups without the occurrence of significant further oxidation to aldehydes or acids is one of the reasons that methane mono-oxygenase (MMO) stands out as an interesting example of a di-iron containing enzyme. The di-iron site in MMO catalyzes the dissociative binding of molecular oxygen. To mimic the MMO active site we work with a finite cluster. We chose to study the binuclear heptapodate coordinated Fe(III)-complexes and characterize them using Mössbauer spectroscopy (MS), quantum mechanics and molecular dynamics modeling and catalysis. Confinement of the active site is required in catalysis in order to modify the behavior of the complex to mimic the MMO enzymatic activity, this can be achieved by depositing the complexes within the voids of mesoporous materials such as HMS or MCM-41 since these materials have large surface areas and large pore sizes. Such hybrid materials can be used in the activation of small molecules as well as larger substrates depending on pore sizes of the mesoporous materials. Inorganic enzyme mimics lack the cooperativity seen in enzymes, so if the mimics come within the 5% of rate of the enzymatic catalysis such effects are marked. $[Fe(IV)_2(=O)2(HPTP)]^{4+}$ has a significantly higher selectivity for the secondary versus tertiary CH bonds in the oxidation of adamantane, such behavior is reminiscent of this observed for MMO, where the selectivity for primary > secondary > tertiary C–H bonds is observed. The $[Fe_2(HPTB)(\mu\text{-}OH)]^{4+}$ complex is generally more selective in oxidation reactions. In solution $[Fe_2(HPTP)(\mu\text{-}OH)]^{4+}$ also shows a higher extent of secondary oxidation of alcohols to consequent oxidation products. The theoretical study of the catalytic hydrocarbon activation of such complexes is studied and the orbital organization of the active sites is probed. Upon activation with oxygen sites of the form $[Fe(III)_2(\mu\text{-}\eta^1\text{:}\eta^1\text{-}O_2)(HPTP)]^{4+}$ (1) and $[Fe(IV)_2(=O)_2(HPTP)]^{4+}$ (2) appear to be active in catalysis. The $\mu\text{-}\eta^1\text{:}\eta^1\text{-}O_2$ mode is slightly lower in energy (more stable) than the O=Fe–O–Fe=O bis-ferryl (reactive site of our model complexes. Overall the reaction with methane is exothermic by 50.56 kcal/mol.

Keywords: Structure–activity relationships; Methane mono-oxygenase; Alkane activation

1. Introduction

Theoretical studies on reactive complexes and enzyme models by Yoshizawa et al. [1], Shilov and Shulpin [2], Noodleman et al. [3] and Siegbahn and Crabtree [4] allow us to get an idea of the complexity of the reactivity of the dinuclear iron cluster active site in methane mono-oxygenase (MMO) that catalyzes the disociative binding of molecular oxygen [4]. Dissociative binding of oxygen via a peroxo intermediate to a diamond core structure leads to a reactive species active in the oxidation of alkanes [5]. MMO and other active sites are among a growing list related to O-

* Corresponding author. Tel.: +32-10-47-29-39; fax: +32-10-47-23-30.
E-mail addresses: ppkg@chim.ucl.ac.be (P.-P.H.J.M. Knops-Gerrits), wag@wag.caltech.edu (W.A. Goddard III).
[1] Tel.: +1-626-395-2731; fax: +1-626-585-0918.

0920-5861/03/$ – see front matter © 2003 Elsevier Science B.V. All rights reserved.
doi:10.1016/S0920-5861(03)00126-3

and OH-bridged di- or poly-iron cores in biological systems [6,7]. MMO has a binuclear active site in which two histidines and four glutarates are present [8]. The crystal structure of a bacterial non-heam iron hydroxylase that catalyses the biological oxidation of methane was determined at 2.2 Å resolution for the 251 K α2β2γ2 dimeric hydroxylase from *Methylococcus capsulatus* (Bath) [9]. Both iron ions in the active site are coordinated by a histidine, an oxygen from a bridging carboxylate and a μ-oxo bridge [9]. In several papers, Lippard and coworkers discussed how such complexes can be made and how the mono-oxygenase transformations are realized [8–11]. Many model complexes have been spectroscopically characterized with Mossbauer, Resonance Raman, NMR, EXAFS and magnetic methods by Que et al., Solomon et al., Girerd, Spiro et al. [12–17,34–37]. Shestakov and Shilov [18] and Schwarz and coworkers [22] made theoretical models of the MMO enzyme active site to study the reaction mechanism involving five-coordinated iron. Noodleman et al. used density functional studies of oxidised and reduced MMO. Their study focuses on the dilemma regarding the identity of the solvent derived bridging ligands within the active site: do they comprise a diiron unit bridged by $1H_2O$ and 1OH– as postulated for *M. capsulatus* (Bath) or 2OH– ligands as postulated for *Methylosinus trichosporium* [3]. The isolation of these various strains of methanotrophs and acidophilic heterotrophic methane-oxidising bacteria allows to construct their phylogenetic trees and take into account their remarkable diversity which may also affect differences in their MMO genes and enzymes [23]. The nature of the oxidized active site with two ferryl groups are these of two reactive two atom centered three electron bonds coupled electronically via a μ-oxo bridge. Its interactions with alkanes is computed using various theoretical methods [19–22] discussed in this paper. The advent of mesoporous materials such as hexagonal molecular sieve (HMS), MCM-41, MCM-48, FSM-16, prepared by ionic and neutral surfactant template pathways opens up new possibilities to study the inclusion of larger complexes than these that can be accommodated in zeolites [24–29]. These materials have large surface areas, high hydrocarbon sorption activities, higher thermal stability and large pore sizes that can be tuned from 1.5 to 10 nm depending on the chain length of the surfactant alkyl group [51–56]. Whereas MCM-41, FSM-16 are prepared via ionic surfactant templating, HMS silica is prepared via hydrogen-bonding interactions between a neutral amine surfactant (S°) and an alkoxide precursor (I°) [51–56]. This allows the formation of mesostructures with thicker walls and smaller crystallite domains for improved access to the framework mesopores. Stable mesoscopic phases can be synthesized under various conditions. The silicon in the framework can be substituted by aluminum in order to obtain alumino-silicates instead of silicates [23–29]. The mimicking of enzymes by immobilization of model complexes in voids of mesoporous silica and silica–alumina has been our ongoing interest [25–29]. In this work, HMS is used for the immobilization of binuclear heptapodate coordinated iron(III)-complexes of *N*,*N*,*N*′,*N*′-tetrakis(2-benzimidazolyl methyl)-2-hydroxy-1,3-diamino-propane (HPTB) and *N*,*N*,*N*′,*N*′,-tetrakis(2-pyridyl methyl)-2-hydroxy-1,3-diamino-propane (HPTP), i.e. $[Fe_2(HPTP)(\mu\text{-}OH)]^{4+}$ (1) and $[Fe_2(HPTB)(\mu\text{-}OH)]^{4+}$ (2). In Figs. 1–10, the characterization of $[Fe_2(HPTP)(\mu\text{-}OH)(NO_3)_2](ClO_4)_2$ (1) and $[Fe_2(HPTB)(\mu\text{-}OH)(NO_3)_2](ClO_4)_2$ (2) with catalysis, Mossbauer spectroscopy and a complimentary theoretical analysis is investigated.

2. Experimental

2.1. Synthesis

2.1.1. $[Fe_2(HPTB)(OH)(NO_3)_2](NO_3)_2$

N,*N*,*N*′,*N*′-Tetrakis(2-benzimidazolylmethyl))-2-hydroxy-1,3-diaminopropane (HPTB, Fig. 5) is prepared after [25,26] by crushing 1,2-diaminobenzene (10.55 g, 0.097 mol) and mixing it to 2-hydroxy-1,3-diaminopropanetetra-acetic acid (5.0 g, 0.016 mol, formed from the diamine and choroacetic acid). The mixture is heated to 170–180 °C for 1 h, till gas formation stops. After cooling the red glassy structure is diluted with HCl (150 ml, 4 M), and a blue precipitate is formed. After filtration the precipitate is washed several times with acetone, dissolved in water and neutralized with a diluted ammonia solution. The white precipitate is recrystallised in acetone, crushed to a fine powder and dried under vacuum. To an ethanol solution of $Fe(NO_3)_3{\cdot}6H_2O$ (0.31 g) the HL (0.30 g) is added. The precipitated iron complex is then collected.

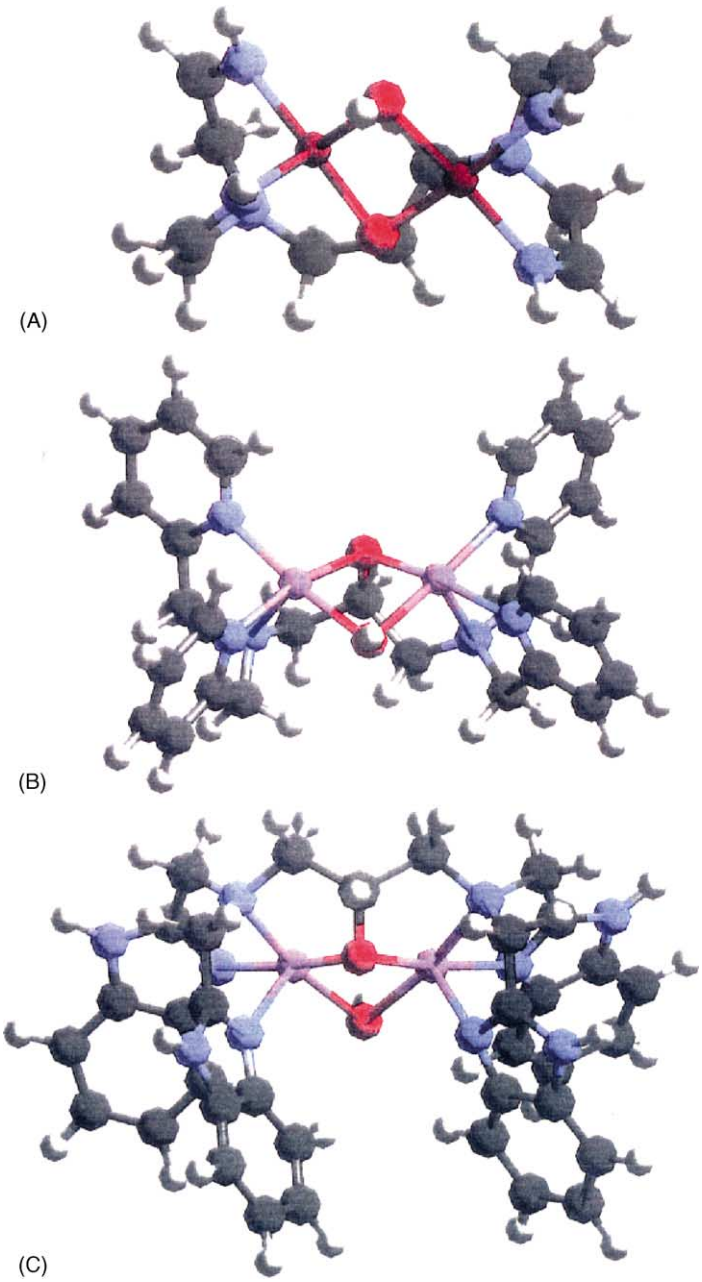

Fig. 1. UFF optimized structure of (A) $[Fe_2(HPTR)(\mu\text{-}OH)]^{4+}$ model compound; (B) $[Fe_2(HPTP)(\mu\text{-}OH)(NO_3)_2](NO_3)_2$ and (C) $[Fe_2(HPTB)(\mu\text{-}OH)(NO_3)_2](NO_3)_2$.

2.1.2. $[Fe_2(HPTP)(OH)(NO_3)_2](ClO_4)_2$

N,*N*,*N*′,*N*′,-Tetrakis(2-pyridylmethyl)-2-hydroxy-1, 3-diamino-propane H(HPTP)* as perchlorate is prepared from *p*-chloropicoline and 2-hydroxy-1,3-diamino-propane after [25,26]. As in the previous synthesis, $Fe(NO_3)_3{\cdot}6H_2O$ (0.31 g) and $H(HPTP)(ClO_4)_2$ (0.28 g) are solved in ethanol to form the complex seen in Fig. 5. The complex is washed with

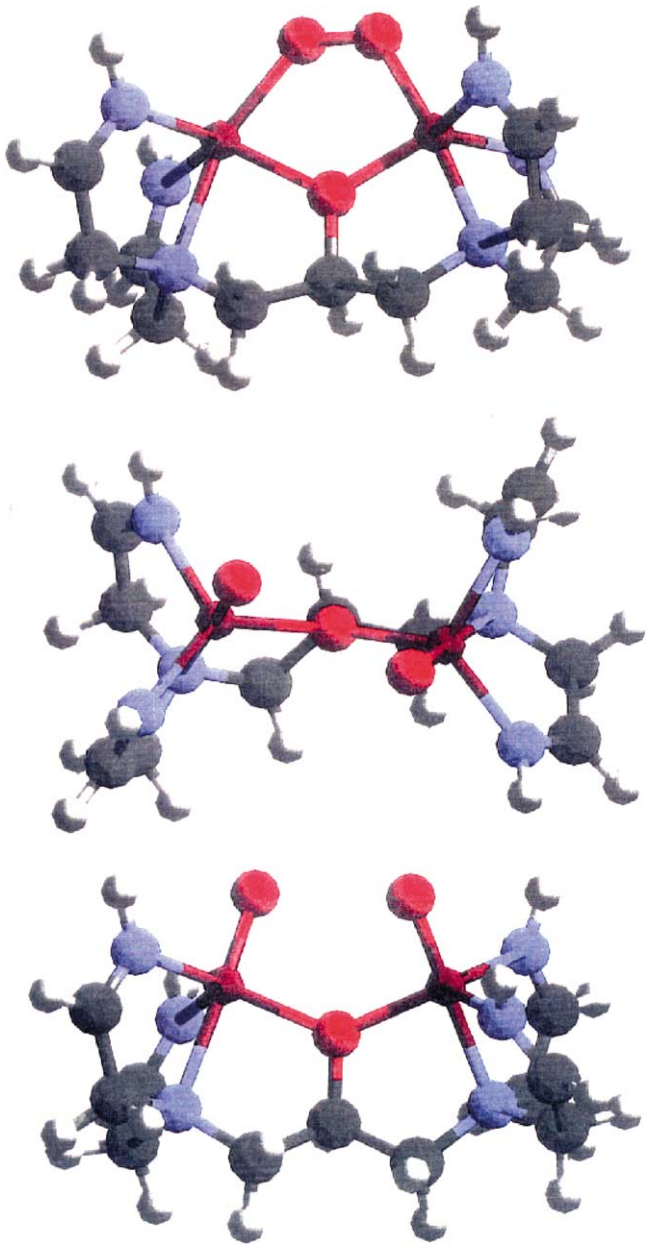

Fig. 2. QM calculated structure of $[Fe_2(HPTR)(\mu\text{-}O_2)]^{3+}$ and $[Fe_2(HPTR)(O)_2]^{3+}$ (top and side) model compounds.

acetonitrile/diethylether and recrystallised in diethylether.

2.1.3. Complex impregnation procedure

To 1 g of HMS support 0.02–0.10 g of the $[Fe_2(HPTB)(OH)(NO_3)_2](NO_3)_2$ or $[Fe_2(HPTP)(OH)(NO_3)_2](ClO_4)_2$ are added in 20 ml CH_3CN to obtain a 2–10% complex loading. The mixture is refluxed in CH_3CN at 85 °C for 35 h to immobilize the cationic complexes and in CH_2Cl_2 at 45 °C for 4 h to remove decomposition products, obtaining yellow powders. The complex occurs in the channels as seen in Fig. 4.

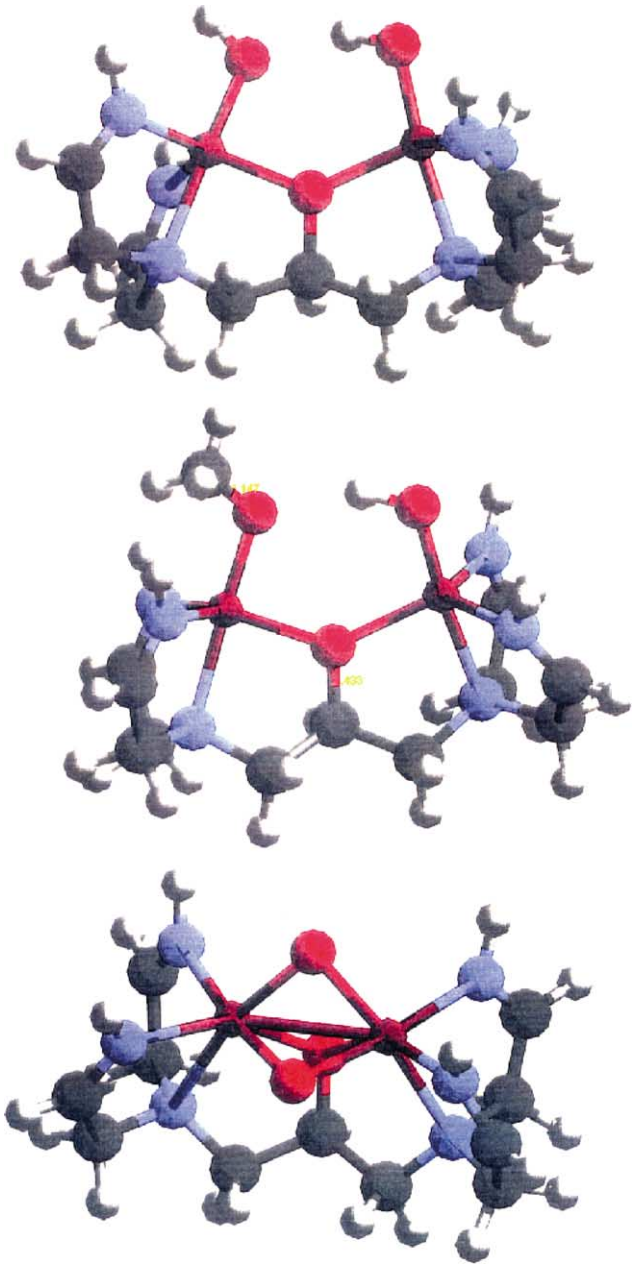

Fig. 3. QM calculated structure of $[Fe_2(HPTR)(OH)_2]^{3+}$, $[Fe_2(HPTR)(OH)(OCH_3)]^{3+}$ and $[Fe_2(HPTR)(\mu\text{-}O)_2]^{3+}$ product compounds.

The use of clays such as montmorillonite as support was reported earlier [24]. The various mesoporous oxide supports are obtained by a procedure described previously for a pure silica MCM-41 [25] and HMS [26]. After filtration of the synthesized mesoporous oxide a white powder is obtained and this white powder is washed with ethanol to remove the template, an additional calcination at 550 °C for 6 h is used.

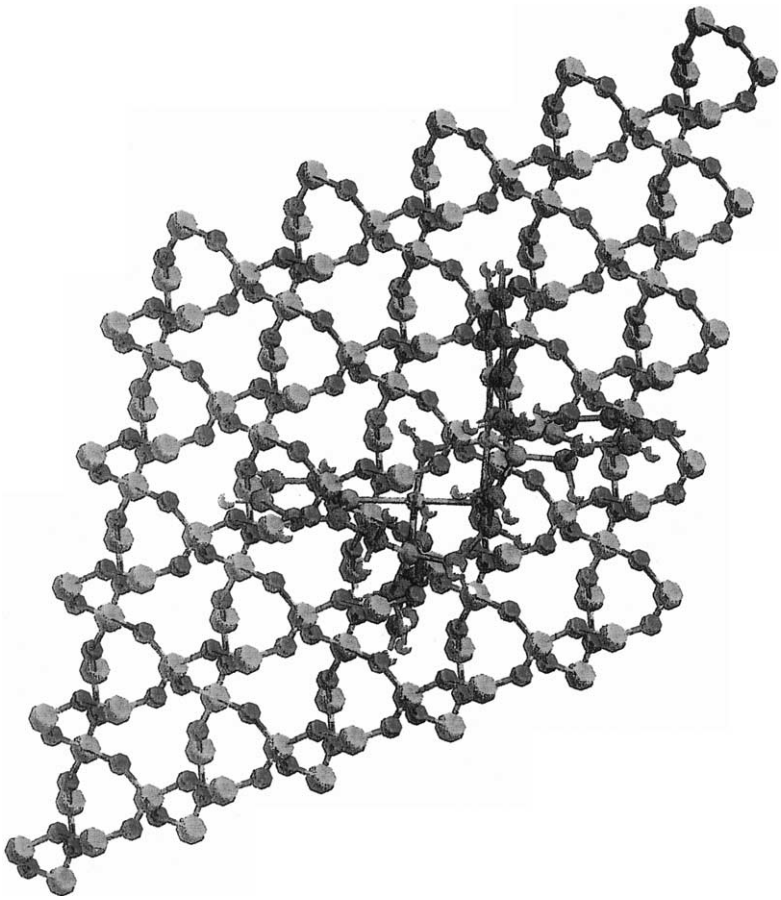

Fig. 4. UFF optimized structure of the $[Fe_2(HPTP)(\mu\text{-}OH)]^{4+}$ model compound on HMS silica within a hexagonal channel with a curved silica surface.

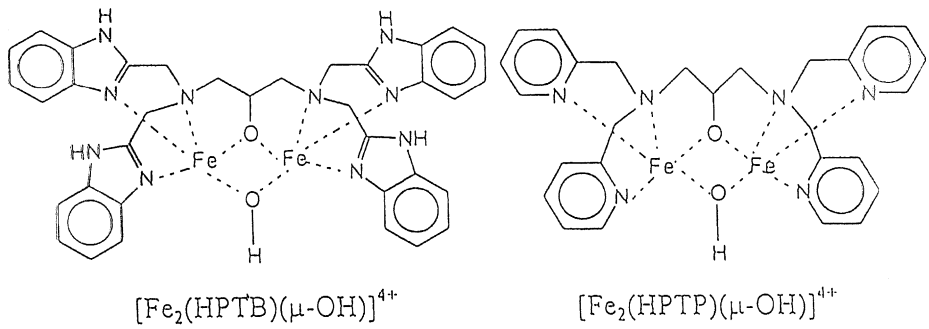

Fig. 5. Schematic structure of the $[Fe_2(HPTB)(\mu\text{-}OH)(NO_3)_2](NO_3)_2$ and $[Fe_2(HPTP)(\mu\text{-}OH)\ (NO_3)_2](ClO_4)_2$ complex cores without the coordinated anions.

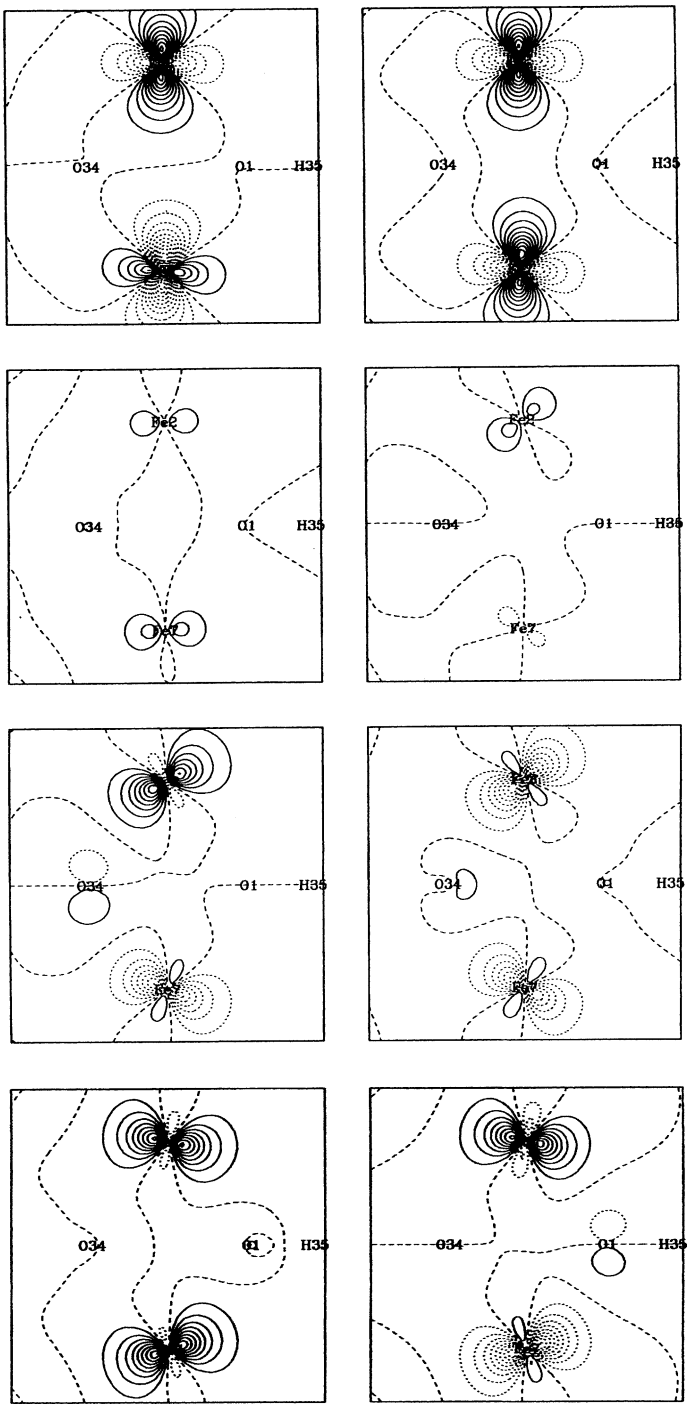

Fig. 6. Orbital maps of the different non-bonding d-shell orbitals seen in the $Fe_2(CO)(OH)$ square of the $[Fe_2(HPTR)(OH)]^{3+}$ complex.

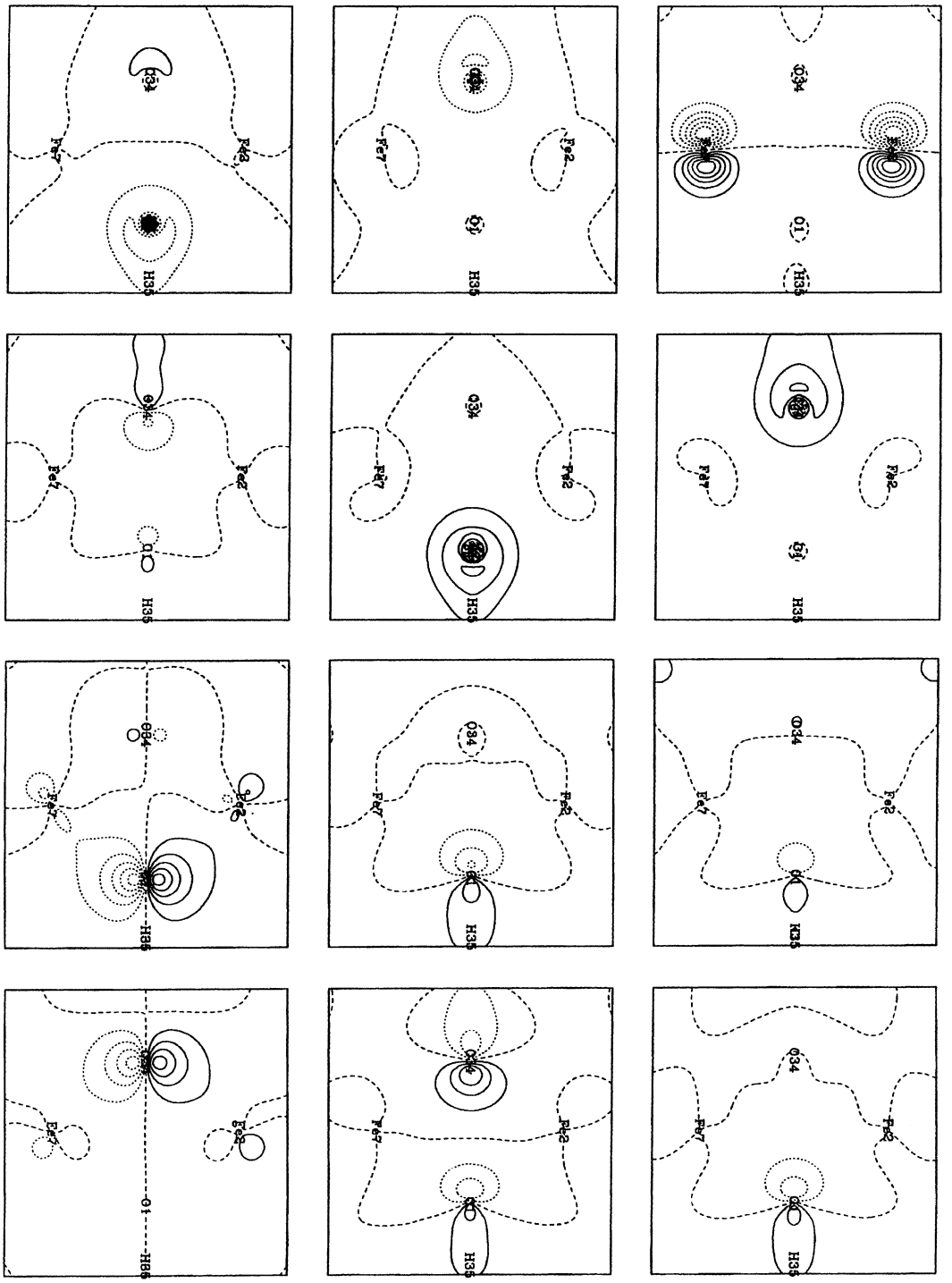

Fig. 7. Orbital maps of the different bonds seen in the $Fe_2(CO)(OH)$ square in which CO is the deprotonated alcohol group of the HPTR ligand of the $[Fe_2(HPTR)(OH)]^{3+}$ complex.

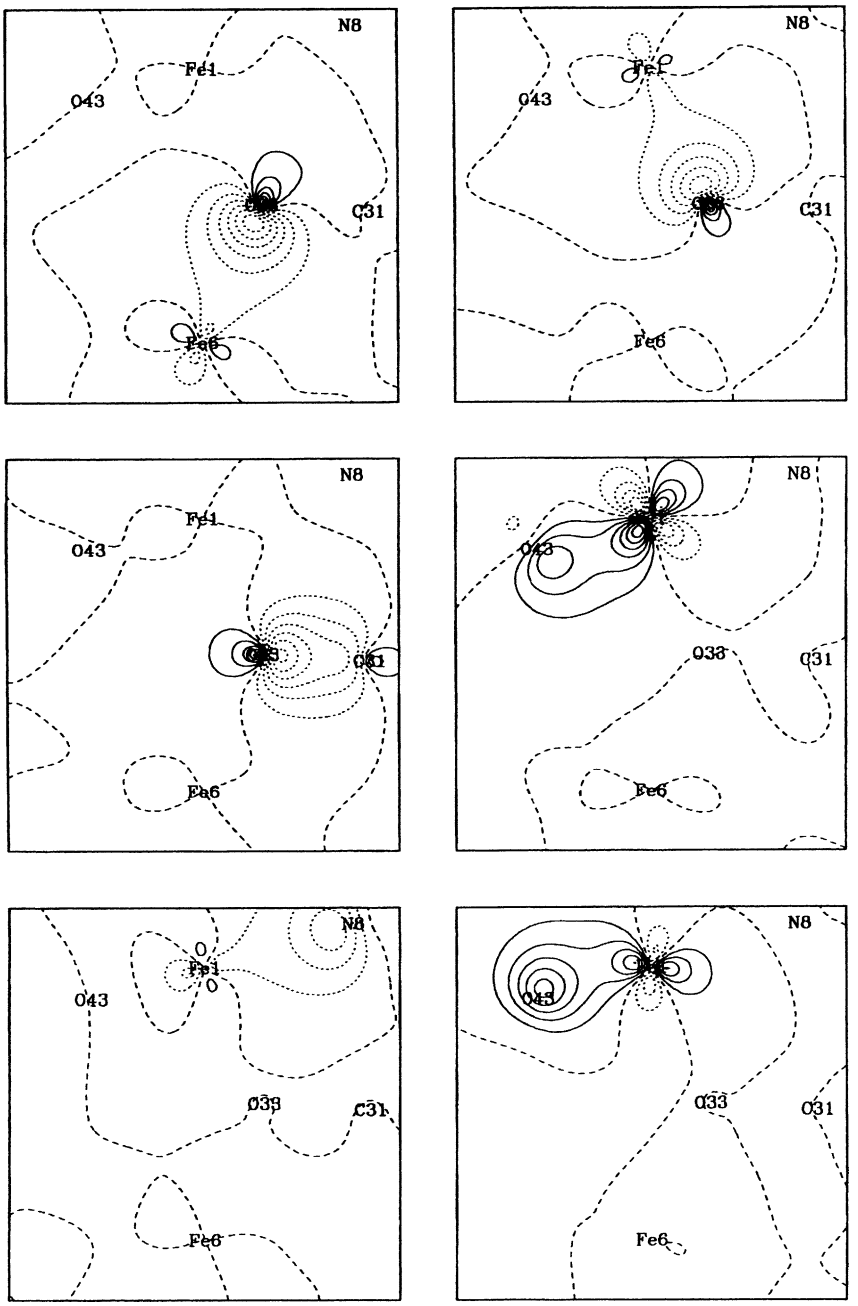

Fig. 8. Orbital maps of the different bonds seen in the Fe–O–Fe=O plane of the $[Fe_2(HPTR)(O)_2]^{3+}$ intermediate.

2.2. Characterisation

Mössbauer spectra are recorded on a vertical constant acceleration drive in transmission geometry with a 28 mCi ^{57}Co(Rh) source. The 14.4 keV Mössbauer transition of the lowest excited level of ^{57}Fe to its ground state ($E_e - E_g = 14.4$ keV, $t_{1/2} = 98$ ns and natural linewidth $= 4.7 \times 10^{-9}$ eV) is fed by the

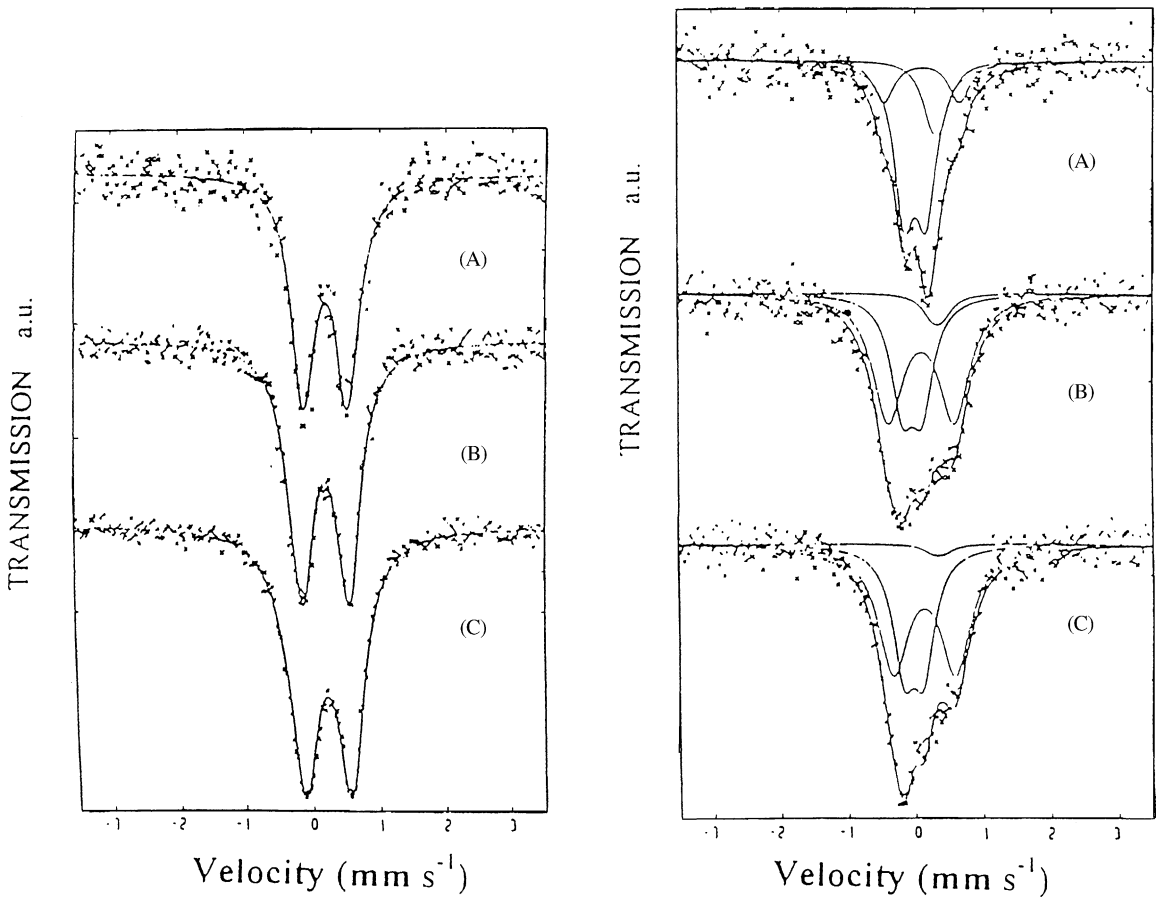

Fig. 9. Mössbauer spectra of $[Fe_2(HPTB)(\mu\text{-}OH)(NO_3)_2](NO_3)_2$ at (a) 293, (b) 100 and (c) 4 K with δ (mm/s) relative to metallic Fe for which $\delta_{me\text{-}Fe} = \delta_{\alpha\text{-}Fe} - 0.0888$ (mm/s) (A). Mössbauer spectra of $[Fe_2(HPTB)(\mu\text{-}OH)]^{4+}$-HMS at (a) 293, (b) 100 and (c) 4 K with δ (mm/s) relative to metallic Fe (B).

decay of the ^{57}Co ($t_{1/2}$ = 270 days). MS is a microscopic, nuclear technique, based on the recoilless emission and absorption of γ-rays by a 'source' and an 'absorber' [30–33]. MS determines the recoilless fraction (or f-fraction) and the hyperfine parameters (isomeric shift δ, quadrupolar splitting Δ and the magnetic splitting) of the MS-nucleus.

Product analysis was done with HP GC on a 50 m CP Sil-5 (dimethylpolysiloxane), 88 (cyanopropylpolysiloxane) or CP Sil-WAX-52 CB (polyethylene glycol) capillary column (Chrompack, 0.32 mm i.d., 1.2 μm film thickness) equipped with FID-detection. GC–MS on reaction mixtures was performed with a GC8000 GC and FISONS MD800 Mass-Spectrometer in CI+ (=positive chemical ionization) or EI mode with a 60 m DB-5MS column (J&W, 0.32 mm i.d., 1 μm film thickness) to confirm the product composition, for all following procedures the analysis is performed analogously.

2.3. Computation

For charge equilibration used in molecular dynamics simulations the charges in the complexes were determined [19]. The molecular mechanics calculations involve a new molecular mechanics force field, the universal force field (UFF). The force field parameters are estimated using general rules based only on the element, its hybridization and its connectivity. The force field functional forms, parameters, and generating

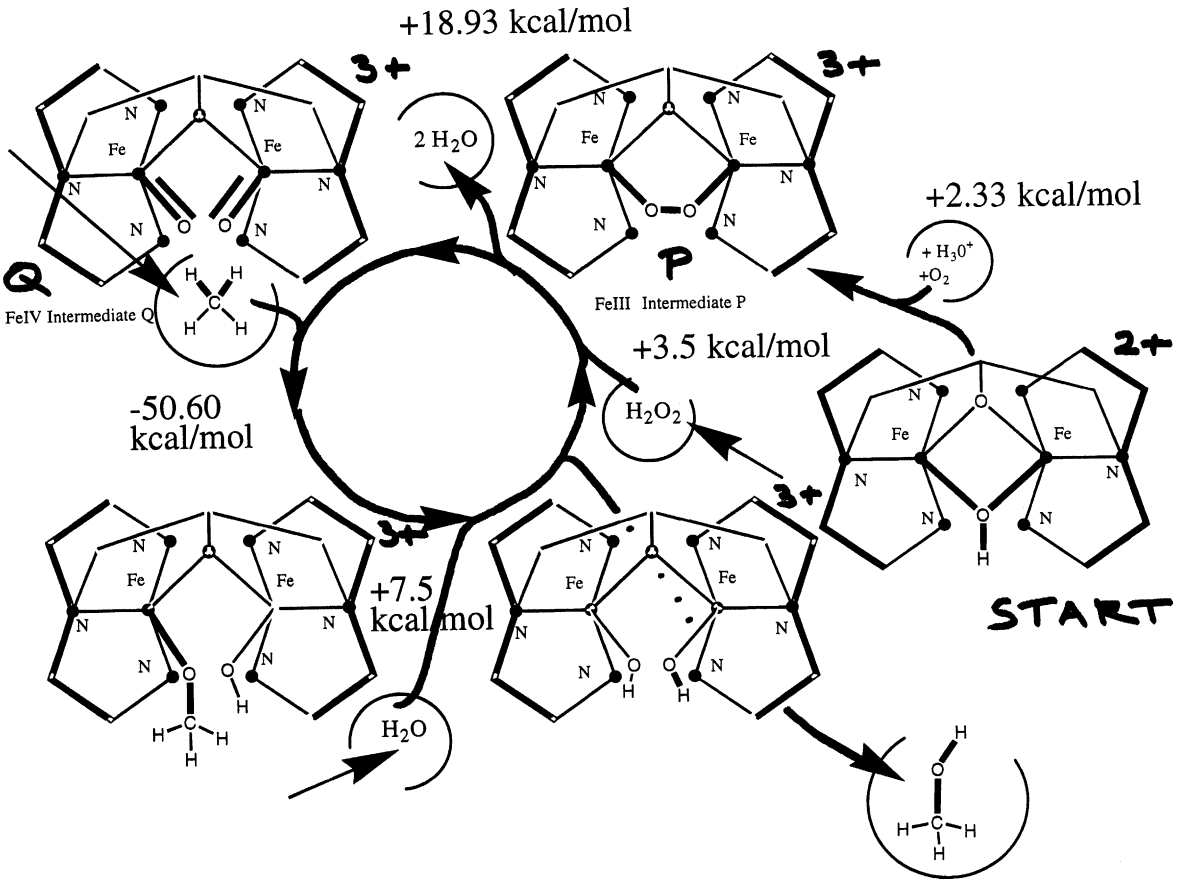

Fig. 10. Reaction scheme of the partial oxidation chemistry with the different intermediates implicated in the catalytic C–H activation by the model complexes.

formulas for the full periodic table have been published [20]. This can help to readjust the charges based on geometry and experimental atomic properties.

The initial structures were energy minimized using a suitable set of parameters that can be appended to the UFF. These can better describe the respective coordination around iron in the model compounds. The quantum mechanical study was then performed at the ab initio level starting from a UFF optimized structure. Conformational structures are compared with the experimental results obtained from the EXAFS analysis.

The ab initio calculations used involve full geometry optimization of the clusters with density functional theory (DFT) as implemented in Jaguar (Jaguar 3.0, Schrodinger Inc., Portland, OR, 1997) at the B3LYP method level (Becke3 hybridization functionals, Slater/Becke88 nonlocal exchange and Li, Yang, Parr local and nonlocal correlation corrections to the local potential energy functionals of Vosko, Wilk and Nusair) using the Los Alamos effective core potential and valence double zeta for iron (LACVP basis sets). Computations are carried out on an Origin2000 (16 MIPS R10000 (IP27) CPU's, 195 MHz w/4 MB secondary cache each, with an IRIX 6.4_S2MP + OCTANE operating system). In order to accommodate the iron in its five coordinate form, as predicted by the EXAFS data, after the UFF optimization a QM calculation was performed. Atom types for iron and other transition metals in the UFF is given with its symbol, hybridization geometry and valence state. UFF contains 126 atom types [20].

Similar to empirical nonreactive force field, the reactive force field (ReaxFF) uses the relationship between bond distance and bond order on the one hand and between bond order and bond energy on the other hand [20,21]. The UFF and ReaxFF predict the potential energy for an arbitrary geometry, the sum of the two, three, four and multi body terms need to be taken into account. The bond stretches are described here as harmonic oscillators. The bond length used is the sum of the atom type specific single bond radii, plus a bond order correction and an electronegativity correction. The force constants are generated using Badgers rules as described [20,21]. The van der Waals parameters are computed based on a Lennard–Jones or Morse type potential. The ReaxFF is currently used to describe the stability and geometry of (non)conjugated and radical-containing compounds and to describe the dissociation and the formation of chemical bonds in hydrocarbon compounds. Since ReaxFF is much faster than conventional quantum-chemical and semi-emperical methods it is easy to use to simulate the formation and dissociation of chemical bonds in large hydrocarbons [21].

The use of atom under- and overcoordination allows to exceed the values of bond order for carbon of four and of hydrogen of one, by allowing it, but imposing a penalty such that the overcoordination energy quickly vanishes, in case of under-coordination the energy contribution of the resonance of the p-electron between attached undercoordinated centers is taken into account [21].

3. Result and discussion

3.1. Mössbauer spectroscopy (MS)

For these iron complexes Mössbauer spectroscopy allows to asses (1) oxidation and spin states of the iron atoms, (2) exchange coupling for diiron at different oxidation levels, (3) valence (de)localisation for mixed-valence complexes [3]. The original and decomposed Mössbauer spectra of $[Fe_2(HPTB)(\mu\text{-}OH)(NO_3)_2](NO_3)_2$ at different temperatures are shown in Fig. 6a. The effect of the interaction of $[Fe_2(HPTB)(\mu\text{-}OH)(NO_3)_2](NO_3)_2$ on HMS in the original and decomposed Mössbauer spectra can be seen in Fig. 6b. Isomer shifts and quadrupole splitting are given in Table 1. Isomer shifts (IS, δ (mm/s) relative to metallic iron at 300 K) are in the range of 1.30 mm/s for Fe(II)Fe(II) MMOH, of the peroxo intermediate P it is in the range of 0.67 mm/s [12], for Fe(III)Fe(III) MMOH it is close to 0.50 mm/s and for Fe(IV)Fe(IV) MMOH the δ value is in the range of 0.17 mm/s for the bis-ferryl intermediate Q [12]. Other model systems show a δ value of 0.35–0.60 mm/s characteristic of 5- or 6-coordinate high-spin diferric μ-hydroxo complexes. Tetrahedral high-spin ferric iron has lower δ value in the range of 0.22 mm/s. For isolated ferric iron ($S = 5/2$) δ values of 0.34 mm/s are seen [33]. In diferric complexes the quadrupole splitting for μ-oxo complexes and μ-hydroxo complexes is larger than 1 mm/s in the former and lower than 1 mm/s in the latter case. The

Table 1
Mössbauer parameters as function of temperature for $[Fe_2(HPTB)(\mu\text{-}OH)(NO_3)_2](ClO_4)_2$ (1) and $[Fe_2(HPTB)(\mu\text{-}OH)]^{4+}$-HMS (2)

Parameters	(1)	(2)			T (K)
δ (mm/s)	0.3161 (36)	0.1128 (14)	0.1968 (16)	0.4348 (24)	293
Δ (mm/s)	0.6466 (62)	0.318 (3)	1.115 (65)	0.145 (91)	
Γ (mm/s)	0.4247 (98)	0.363 (40)	0.373 (81)	0.360 (–)	
Relative intensity (%)	100	61	19.5	19.5	
δ (mm/s)	0.2896 (23)	0.0608 (20)	0.1898 (8)	0.4288 (–)	100
Δ (mm/s)	0.6875 (40)	0.287 (14)	0.966 (28)	0.15 (–)	
Γ (mm/s)	0.4405 (63)	0.398 (43)	0.546 (26)	0.360 (–)	
Relative intensity (%)	100	36	59	5	
δ (mm/s)	0.2996 (17)	0.0608 (15)	0.2198 (9)	0.4338 (290)	4.2
Δ (mm/s)	0.6940 (29)	0.290 (–)	0.915 (38)	0.150 (–)	
Γ (mm/s)	0.5109 (49)	0.392 (43)	0.548 (29)	0.360 (–)	
Relative intensity (%)	100	39	59	2	

δ Relative to α-Fe.

reduction in electric field gradient, indicated by the smaller QS in the hydroxo-bridged complexes may be due to the lengthening of the Fe–O bond upon protonation of the oxo bridge. This is a trend seen for both di- and tribridged complexes. The QS is also sensitive to changes in the coordination sphere.

In $[Fe_2(HPTB)(\mu\text{-}OH)(NO_3)](NO_3)_2$ all of the iron (QS1) is present as coordinated high-spin ferric iron with a δ value of 0.32 mm/s that is rather low, and lies below the values of 0.50 mm/s for Fe(III)Fe(III) MMOH. The value of 0.65 mm/s for the QS points to μ-hydroxo-type complexation. From the variable-temperature ^{57}Fe Mössbauer characteristics there is little change in the localized electronic structure as the temperature is increased from 4.2 to 293 K. This agrees with the calculations that show that an intermediate spin coupled state is observed at 4.2 K, that does not significantly increase upon heating.

For $[Fe_2(HPTB)(\mu\text{-}OH)]^{4+}$ in HMS 59% of the iron is present as Fe(III) species with a δ value of 0.22 mm/s. The other 39% has a reduced a δ value of 0.06 mm/s and a QS of 0.29 mm/s can be assigned to Fe(III) or Fe(IV). The temperature-sensitivity of the Mössbauer characteristics is a result of the changes in the f-fraction of the iron in different valence, symmetry or environment. The interaction of lattice oxygen atoms with the μ-hydroxo bridge may lead to H-bonding and a decreased QS. Alternatively, 5-compared to 6-coordinated binuclear centers may show significantly higher QS, as the less symmetrical trigonal–bipyramidal Fe(III) site has a higher QS compared to the octahedral Fe(III) site. This explanation is likely as removal of charge compensating NO_3^- groups, reduces the coordination symmetry of the Fe(III) core. Furthermore calculations favor 5- over 6-coordinated binuclear centers for ferric iron [1]. The observed increase of the line-width from 0.42 mm/s for equivalent iron sites to the value of 0.88 mm/s indicates a decreased degree of equivalence of the two iron atoms. A slight increase of the QS with temperature decrease is typical for high-spin Fe(III) systems due to changes in the Boltzmann populations of the low-lying electronic states that form as a consequence of spin-orbit and low-symmetry crystal field perturbations.

In $[Fe_2(HPTP)(\mu\text{-}OH)(NO_3)](ClO_4)_2$ the distribution of iron species is more complex and was previously discussed [25]. Coordination with the heptadentate ligand occurs through a tripodal nitrogen and single alkoxy-complexation. The μ-oxo-bridged synthetic di-iron complexes show temperature-dependant variations in their spin state, due to a transition from anti-ferromagnetism at low temperatures to paramagnetism at more elevated temperatures. For the μ-hydroxo-bridged synthetic di-iron complexes this behavior seems less pronounced.

The interactions of lattice O or OH of HMS with iron complexes is less pronounced when bulkier ligands e.g. HPTB shield the active site better from the surface and this serve as explanation for the two species seen in the Mossbauer spectra, one closer to a μ-OH, one closer to a μ-O species. The interaction of the Lewis base lattice μ-O site with a μ-OH of the complex may occur. The μ-oxo/μ-hydroxo-bridged synthetic di-iron complexes show a lengthening of the iron-iron distance on HMS of about 0.2 Å as previously determined by EXAFS studies on the heterogenisation of these complexes [29]. The implications on the oxygen dissociative binding are such that the μ-η1-η1 peroxo will less likely split homolytically, and the bound peroxo may be more active in singlet oxygen type dioxygen insertion reactions.

3.2. Computational analysis

3.2.1. Modeling the structures

The UFF optimized $[Fe_2(HPTP)(\mu\text{-}OH)]^{4+}$ (1), $[Fe_2(HPTB)(\mu\text{-}OH)]^{4+}$ (2) and $[Fe_2(HPTM)(\mu\text{-}OH)]^{4+}$ with M = model C=N in stead of pyridine or imidazole (3) are shown in Fig. 1. Both the ferric $[Fe_2(HPTM)(\mu\text{-}OH)]^{4+}$ and the ferrous $[Fe_2(HPTM)(\mu\text{-}OH)]^{2+}$ cores were then optimized with QM. The QM optimized structure of $[Fe_2(HPTM)(\mu\text{-}OH)]^{4+}$ is reacted with oxygen in an acidic medium to give intermediates P and Q as shown in Figs. 2 and 3. As explained further their interactions with H_2 and CH_4 are studied as shown in Fig. 3.

The bond lengths and angles obtained by UFF and QM calculations (HPTB, HPTP, HPTM, M = model C=N in stead of Py or Im) are shown in Tables 2 and 3. The UFF bond stretch types, angle bending types and Lennard–Jones 12–6 parameters for the model complexes are used. Due to the change of a ferrous type to a ferric type the decrease in the bond-length and the increase in the force constant for the Fe–X distances are seen. Furthermore, some changes in the

Table 2
Bond lengths obtained by UFF and QM calculations on the $[Fe_2(OH)(HPTR)]^{4+}$ complexes in which HPTM is a model ligand that has four C=N groups in place of either four pyridine (HPTP) or four benzimidazole (HPTB) groups

Bond lengths (Å)	HPTB, UFF	HPTP, UFF	HPTM, UFF	HPTM, QM
Fe–Fe	2.938	2.939	2.940	3.135
Fe–O_1	2.021–2.028	2.024	2.024	1.991–1.992
Fe–O_2	2.012–2.008	2.009	2.010	1.949–1.950
Fe–N (sp^2)	2.051–2.062	2.076–2.077	2.068–2.077	2.030–2.041
Fe–N (sp^3)	2.088–2.106	2.081	2.056	3.120
C–C	1.410–1572	1.398–1.568	1.519–1.568	1.502–1.544
N–H (sp^2)	1.044	–	1.030	1.028
N (sp^2)–C	1.332	1.357	1.288	1.288
N (sp^3)–C	1.511	1.498	1.479	1.511
O_1–H_1	0.990	0.990	0.990	0.978
C_1–O_2	1.454	1.452	1.452	1.427
C–H	1.082–1.111	1.082–1.112	1.086–1.110	1.095–1.100

angle bending parameters can be observed. The angles for the Fe–O–H and Fe–O–C increase from the standard 110–128.0 and 126.4° in the diferric core. Also, a decrease of the O–Fe–O angle can be seen from 90 to 74.5°. The N–Fe–N angles for the two equatorial N atoms rise to 110° and for an equatorial N and an axial N decrease to 78–79°.

The bond lengths and angles obtained by QM calculations for all the intermediates in the catalytic cycle of the $[Fe_2(HPTM)(\mu\text{-}OH)]^{X+}$ cluster (the charge X is +4 or +2) are shown in Tables 4 and 5. Relative and absolute energies of important catalytic intermediates obtained by QM calculations are analyzed. Simulation of Fe(III) and Fe(II) active sites allow us to obtain the energy levels of different multiplicity as shown in Table 6. Effects of solvation from QM calculations vary largely with the charge of the clusters as seen in Table 7. Alkanes like methane have a negative solvation energy difference, charged peroxo type intermediates may show large positive solvation energy differences.

The complex has C_{2h} symmetry and both ferrous iron ions can occur either in a high-spin quintet state, and intermediate-spin triplet state and a third state, the low-spin singlet state, when these states couple we obtain the nonuplet state

$$N = (dxz)^2(dxy)^1(dyz)^1(dz^2)^1(dx^2 - y^2)^1$$

if the two iron ions are high-spin, the quintet state Q

$$Q = (dxz)^2(dxy)^2(dyz)^1(dz^2)^1$$

if the two iron ions are intermediate-spin, or singlet

$$SI = (dxz)^2(dxy)^2(dyz)^2$$

when the two iron ions are in low-spin form.

When both ferric iron ions can occur either in a high-spin quintet state, and intermediate-spin triplet

Table 3
Bond angles obtained by UFF and QM calculations for the $[Fe_2(OH)(HPTR)]^{4+}$ complexes in which HPTM is a model ligand that has four C=N groups in place of either four pyridine (HPTP) or four benzimidazole (HPTB) groups

Bond angles (°)	HPTB, UFF	HPTP, UFF	HPTM, UFF	HPTM, QM
Fe–OH–Fe	93.1	93.2	93.1	103.823412
Fe–O–Fe	93.9	93.9	93.8	107.026004
O–Fe–O	80.5–80.6	80.6–80.7	80.4–80.5	74.551–74.509
H–O–Fe	104.4–104.6	104.5–104.6	104.6–106.1	127.999–128.170
C–O–Fe	104.4–105.2	104.5–105.3	95.7–109.6	126.291–126.530
N_e–Fe–N_e	89.8–93.5	89.8–93.1	90.1–93.3	110.0
N_a–Fe–N_e	83.9–83.5	82.2–82.5	84.3–84.3	78.3–78.9

N_e is a N at equatorial position and N_a is a N at axial position.

Table 4
Bond lengths obtained by QM calculations for the model complexes observed throughout the catalytic cycle with various oxo, hydroxo, peroxo and methoxy ligand groups as well as the HPTM ligand has C=N groups that substitute for the pyridine or benzimidazole groups in the real ligand

Bond lengths (Å)	$[(Fe{=}O)_2$ (HPTM)$]^{3+}$, QM	$[Fe_2$ (HPTM) $(\mu\text{-}\eta^1{:}\eta^1\text{-}O_2)]^{3+}$, QM	$[Fe_2$(HPTM) $(\mu\text{-}O)_2]^{3+}$, QM	$[Fe_2$ (HPTM) $(OH)_2]^{3+}$, QM	$[Fe_2$(HPTM) $(OH)(OCH_3)]^{3+}$, QM
Fe–Fe	3.628	3.433	2.647	3.639	3.600
Fe–O	1.607–1.611	1.843–2.037	1.824	1.724	1.729
			1.909	1.756	1.747
Fe–O (HPTM ligand)	1.971–1.982	1.876–2.039	2.071	1.958–2.008	1.993–1.993
O–O		1.309			
Fe_a–N (sp^2)	2.020–2.034	2.000–2.085	1.956–2.078	2.093–2.109	2.010–2.072
Fe_b–N (sp^2)		2.093–2.095			2.031–2.071
Fe_a–N (sp^3)	2.101–2.166	2.077	2.056	3.120	2.094
Fe_b–N (sp^3)		2.270			2.107
C–C	1.498–1.507	1.498–1.544	1.495–1.565	1.502–1.544	1.502–1.544
(C=)N–H	1.022–1.024	1.022–1.025	1.023–1.024	1.028	1.028
N=C	1.282	1.280–1.283	1.276–1.282	1.288	1.288
N–C	1.504–1.513	1.493–1.519	1.497–1.503	1.511	1.511
O–H	–	–	–	0.974–0.984	0.974–0.984
C–O (HPTM ligand)	1.437	1.435	1.420	1.433	1.432
C–H	1.097–1.099	1.082–1.112	1.092–1.198	1.094–1.101	1.094–1.101

Table 5
Bond angles obtained by QM calculations on the model complexes observed throughout the catalytic cycle with various oxo, hydroxo, peroxo and methoxy ligand groups as well as the HPTM ligand that has C=N groups that substitute for the pyridine or benzimidazole groups in the real ligand

Bond angles (°)	$[(Fe{=}O)_2(HPTM)]^{3+}$, QM	$[Fe_2(HPTM)(\mu\text{-}\eta^1{:}\eta^1\text{-}O_2)]^{3+}$, QM	$[Fe_2(HPTM)(\mu\text{-}O)_2]^{3+}$, QM	$[Fe_2(HPTM)(OH)_2]^{3+}$, QM	$[Fe_2(HPTM)(OH)(OCH_3)]^{3+}$, QM
Fe–O–Fe	133.2	122.4	79.4–93.0	133.1	133.7
O–Fe–O	97.8–98.7	80.3–89.9	72.2–78.2	93.2–101.9	95.9–99.4
Fe–O–O	–	119.9–123.7	–	–	–
H–O–Fe	–	–	–	113.0–117.1	112.2
C–O–Fe	109.9–116.8	117.9–119.6	116.9	112.2–114.5	112.7–113.3
N_e–Fe–N_e	115.6–115.9	108.9–110.1	118.0	116.9–119.2	117.6–117.8
N_a–Fe–N_e	81.0–81.3	81.7–83.4	80.6–83.9	80.0–80.7	80.2–81.3

N_e is a N at equatorial position and N_a is a N at axial position.

Table 6
Relative energies obtained by QM calculations on active intermediates of the complexes in which HPTM is a model ligand that has four C=N groups in place of either four pyridine (HPTP) or four benzimidazole (HPTB) groups

Species, charge	Absolute energy (Hartrees)	*M*	Spin	Energy difference (kcal/mol)
$[Fe_2(OH)(HPTM)]^{4+}$	−1156.66002520976	1	0	+55.212
$[Fe_2(OH)(HPTM)]^{4+}$	−1156.72103934993	3	1	+16.975
$[Fe_2(OH)(HPTM)]^{4+}$	−1156.73506990023	5	2	+8.171
$[Fe_2(OH)(HPTM)]^{4+}$	−1156.74809101708	7	3	0.000
$[Fe_2(OH)(HPTM)]^{4+}$	−1156.74604606051	9	4	+1.283
$[Fe_2(OH)(HPTM)]^{4+}$	−1156.73649769241	11	5	+7.275
$[Fe_2(OH)(HPTM)]^{2+}$	−1157.76480812098	1	0	+91.696
$[Fe_2(OH)(HPTM)]^{2+}$	−1157.74190823559	3	1	+96.066
$[Fe_2(OH)(HPTM)]^{2+}$	−1157.83278967371	5	2	+39.037
$[Fe_2(OH)(HPTM)]^{2+}$	−1157.85602986274	7	3	+24.454
$[Fe_2(OH)(HPTM)]^{2+}$	−1157.89500007865	9	4	0.000
$[Fe_2(OH)(OCH_3)(HPTM)]^{3+}$	−1272.53142180726	7	3	+47.747
$[Fe_2(OH)_2(HPTM)]^{3+}$	−1233.21734790106	7	3	+75.317
$[Fe_2(\mu\text{-}\eta^1{:}\eta^1\text{-}O_2)(HPTM)]^{3+}$	−1231.91828781009	9	4	0.000
$[(Fe{=}O)_2(HPTM)]^{3+}$	−1231.88812648956	9	4	+18.927
$[Fe_2(\mu\text{-}O)_2(HPTM)]^{3+}$	−1231.84764860580	9	4	+44.327

state and a third state, the low-spin singlet state, when these states couple we obtain the undecuplet state

$$U = (dxz)^1(dxy)^1(dyz)^1(dz^2)^1(dx^2 - y^2)^1$$

if the two iron ions are high-spin, the septet state Q

$$SP = (dxz)^2(dxy)^1(dyz)^1(dz^2)^1$$

if the two iron ions are intermediate-spin, or triplet

$$T = (dxz)^2(dxy)^2(dyz)^1$$

when the two iron ions are in low-spin form.

In the ferric case (Fe(III)) the septet (SP) seems the ground state. The equatorial (*trans*) and axial (*cis*) effect of the N atoms with respect to the bridging μ-oxo

Table 7
Relative solvation energies obtained by QM calculations on active intermediates of the complexes in which HPTM is a model ligand that has four C=N groups in place of either four pyridine (HPTP) or four benzimidazole (HPTB) groups

Species, charge	Absolute energy (Hartrees)	*M*	Spin	Solvation energy difference (kcal/mol)
$[Fe_2(OH)(OCH_3)(HPTM)]^{3+}$	−1273.596854	7	3	327
$[Fe_2(OH)_2(HPTM)]^{3+}$	−1234.245871	7	3	335
$[(Fe{=}O)_2(HPTM)]^{3+}$	−1232.996704	9	4	340
$[Fe_2(OH)(HPTM)]^{4+}$	−1158.653119	9	4	592
$[Fe_2(OH)(HPTM)]^{2+}$	−1158.405161	9	4	155
OH_3^+	−76.70383	1	0	+100.847
OH_2	−76.41973	1	0	
OH	−75.72712	2	1/2	
O_2H_2	−151.55854	1	0	
O_2H^-	−150.95229	1	0	+97.032
O_2	−150.32334	3	1	
O	−75.05850	3	1	
H_2	−1.17897	1	0	
H	−0.50027	1	0	
CH_4	−40.524047	1	0	−5.000
CH_3OH	−115.721813	1	0	

groups dictate their bond lengths that are 2.03–2.04, 2.31 and 1.95–1.99 Å, respectively. The elongation of the bond distances of 2.01–2.03 Å seen in the UFF calculations shown in Table 2 in the direction of the equatorial O and OH groups compared to the 1.95 and 1.99 Å distances obtained from QM calculations, are due to a decrease of the Fe–O–Fe angle from 107.0 to 94° and due to a increase of the O–Fe–O bite angle from 74.5° in QM compared to 80–81° in UFF as shown in Table 3. The bond shortening to 2.05–2.11 Å observed in the direction of Fe to the axial N group obtained by UFF calculations, differs from longer bond distances of 2.31 Å seen in QM calculations and are due to a decrease of the N–Fe–N bite angle from 110.0° in QM to 90° in UFF. In UFF the order of the angles is such that Fe–O–R > Fe–N–R > N–Fe–N > Fe–O–Fe > O–Fe–O whereas in QM the order of the angles is such that Fe–O–R > Fe–N–R > Fe–O–Fe–N–Fe–N > O–Fe–O, in particular the first two values are much higher in QM compared to UFF and the last two values are much lower in QM compared to UFF. Such changes in the UFF parameters allow to better position HPTB and HPTP ligands. Larger systems can be studied with QM-parametrized modified UFF parameters.

3.2.2. *Modeling the oxygen activation*

Geometrical and electronic properties as shown in Fig. 3 affect the relative catalytic properties as shown in Fig. 7 such as the H-bond abstraction energies from C–H bonds by binuclear iron complexes. In the QM optimized structure the iron core has two μ-oxo and six terminating nitrogen atoms. In aqueous reactions using acidic media, bridging by the deprotonated ligand alcohol group is strong, whereas the bridging (μ-OH) can be protonated and removed as water and lead to a vacant site that allows the binding of molecular oxygen and consequent transformation of this intermediate into an oxidized bis-ferryl form. During this transformation the oxygen molecule is transformed in a peroxo (O_2^{2-}) group (intermediate P) with the formal change of the charges of iron from +2 to +3.

This leads to a diamagnetic singlet state

$$S = (dxz)^2(dxy)^2(dyz)^1(O_2\pi)^1(dz^2)^1(O_2\sigma)^1$$

here the d*yz* orbital is coupled to the two orthogonal three electron pi-system of the O_2 ligands. The alternative is a paramagnetic quintet state

$$Q = (dx^2 - y^2)^1(dxz)^2(dxy)^1(dyz)^1(O_2\pi)^1(dz^2)^1 \times (O_2\sigma)^1$$

The two double ferryl type bonds can become stronger by transfer of the sigma bonding electrons between the two oxygen atoms to their anti-bonding orbitals and the pairing of these with an extra electron from the iron ion.

In a consequent step the peroxo (O_2^{2-}) group is transformed into two ferryl (O^{2-}) bound groups (intermediate Q), with the formal change of the charges of iron from +3 to +4. In an alternative step the peroxo (O_2^{2-}) group of the complex can also transform to yield two bridging (μ-O) oxo groups, additional to the ligand bound O, which remains coordinated.

The ferrous complexes show a lower energy compared to the ferric complexes with a difference of about 719.7 kcal/mol. Whereas for the diferric complex the intermediate spin seems to be the ground state for the diferrous complex the high-spin state is the ground state as can be seen in Table 6. From these calculations it is clear that the super-exchange coupling for these complexes is fairly small, this agrees with the experimental observation of a *J* value of 12 cm^{-1} for the diferrous OH bridged model compound [16,17].

The geometrical implications on these reactions are probed with QM analysis and the results are shown in Tables 4 and 5. The oxygen bond length of 1.21 Å increases to 1.31 Å on the model compound and is smaller than the 1.49 Å distance in hydrogen peroxide, consequently this bond is broken in the model compound. The Fe–Fe distances in the model compound of 3.14 Å increases to 3.43 Å in intermediate P and 3.63 Å in intermediate Q. Upon transformation into the bis (μ-O^{2-}) oxo bridged dimer, this distance decreases to 2.65 Å. The energetics of these different intermediates seem fairly comparable with the peroxo form or intermediate P, being slightly more stable than the ferryl form or intermediate Q by about 18.9 kcal/mol. The formation of the bis (μ-O^{2-}) oxo seems unfavorable since it is 44.4 kcal/mol higher in energy. However, solvation stabilization might be higher in the complexes with increased charge transfer i.e. the Fe(IV) complexes may be better stabilized by solvation than the Fe(III) complexes.

3.2.3. Modeling the alkane activation

Upon interaction with CH_4 the geometry of the two ferryl (O^{2-}) bound groups (intermediate Q) to the ferric (Fe(III)–OH) and ferrous groups does not change substantially in the N terminated model clusters, whereas the Fe–Fe distances remain the same i.e. 3.63 and 3.64 Å, the Fe–O distances change, as the system becomes more asymmetric since one OH group that is formed will show hydrogen bonding with the neighboring methoxy group. For an excited state with the bridging Fe–O distances change from 1.97 and 1.96 Å to 2.002 and 1.975 Å and the terminal Fe–O distances increase from 1.61 and 1.61 Å to 1.748 (Fe(III)OH) and 1.723 Å (Fe(III)OCH_3), the CH and OH distances are 1.097, 1.096, 1.094 and 0.982 Å, respectively. For the ground state the bridging Fe–O distances change from 1.97–1.96 Å to 1.993–1.993 Å and the terminal Fe–O distances increase from 1.61 and 1.61 Å to 1.747 (Fe(III)OH) and 1.729 (Fe(III)OCH_3) A, the CH and OH distances are 1.097, 1.096, 1.095 and 0.982 Å, respectively. The multiplicity nine ($Fe_2(N)_6(O)_2$(μ-OL)(=O)$_2$) and 7 ($Fe_2(N)_6(O)_2$(μ-OL)(OCH_3)(OH)) cases are symmetrical and asymmetrical. Upon interaction with H_2 the hydrogen bonding also occurs and the bridging Fe–O distances change from 1.97–1.98 Å to 1.96–2.00 Å and terminal Fe–O distances increase from 1.61 to 1.72–1.76 Å, the OH distances are 0.97 and 0.98 Å, respectively.

Overall the reaction with methane is exothermic by 50.56 kcal/mol as seen in Fig. 7, the consecutive substitution of the methoxy group by a hydroxo group is endothermic by 7.50 kcal/mol and the regeneration of the active site with H_2O_2 is again endothermic by 3.24 kcal/mol. The solvation calculations are very important to obtain good quantitative data. The solvation energy is about 150, 300 and 600 kcal/mol for the 2+, 3+ and 4+ complexes, respectively as can be seen in Table 7.

The energetics of the reduction obtained with the model clusters can be considered as two subsequent H adduct steps. The overall reaction starting from the two ferryl (O^{2-}) bound groups is exothermic by about 94.3 kcal/mol. Thus, with an energy content of 112 kcal/mol H_2 and the formation of two OH groups of 102 kcal/mol, apparently rather weak π-bonding in the ferryl species seems to occur. The charges in the product compounds are shown in Tables 8 and 9.

Table 8
Charges of the atoms of active intermediate Q with active site of the form $[(Fe{=}O)_2(HPTM)]^{3+}$ and calculations of the complex from QC and QEq*

	QC_{ESP}	QeqN*
Fe	+1.158, +1.188	+1.104, +1.116
–O–	−0.765	−0.443
O=	−0.290, −0.301	−0.425
H	+0.420, +0.050	+0.191, +0.050
N	−0.704, −0.621	−0.285, −0.275
N	+0.466, +0.363	−0.419, −0.409
C	−0.447, −0.498	−0.137, −0.128
C (–O–)	+0.364, +0.321	+0.110

Electronegativies where modified to XFe = 3.5, X_O = 8.741, X_C = 5.343, X_N = 6.899, X_H = 4.528, the hardness and radius for Fe were modified to 1/2 J_{Fe} = 3.124 and R_{Fe} = 1.293, respectively.

3.2.4. Description of the orbitals involved in the reactive site

From a geometrical point view the starting complex can be considered to consists of two $Fe(N)_3(O)$ fragments that share two oxygen ions, one from the μ-oxo-C bridge of the ligand (OL) and one from a μ-hydroxo bridge, to form a $Fe_2(N)_6(O)_2$ (μ-OL)(μ-OH) active site. The $Fe_2(N)_6(O)_2$ fragment has four non-bonding orbitals. We can thus consider the side-on and end-on di-oxygen coordination on the $Fe_2(N)_6(O)_2$ fragment. This will be discussed further. The frontier orbitals for the starting complex shown in Figs. 8 and 9 are derived from the iron core with a μ-oxo-C ligand bridge and a μ-hydroxo group as

Table 9
Charges of the atoms of product species with active site of the form $[Fe_2(OH)(OCH_3)(HPTM)]^{3+}$ and calculations of the complex from QC and QEq*

	QC_{ESP}	QeqN*
Fe	+1.143, +1.249	+1.008, +1.032
–O–	−0.959	−0.454
R–O–	−0.568, −0.675	−0.540, −0.654
H	+0.153, +0.461	+0.100, +0.098
N	−0.726, −0.696	−0.290, −0.272
N(NC2H)	+0.408, +0.317	−0.416, −0.401
C	−0.433, −0.009 (OCH3)	−0.129, −0.127
C (–O–)	+0.463, +0.321	+0.121

Electronegativies where modified to X_{Fe} = 3.124, X_O = 8.741, X_C = 5.343, X_N = 6.899, X_H = 4.528, the hardness and radius for Fe were modified to 1/2 J_{Fe} = 3.124 and R_{Fe} = 1.293, respectively.

shown in the scheme of Fig. 5. Here we observe that the two Fe and two O ions form a square structure in which various s, p and d orbitals involved are shown. The $Fe_2(N)_6(O)_2$(μ-OL) fragment has two non-bonding orbitals which can react with the O ion to form a μ-(hydr)oxo bridge, since the non-bonding orbitals lie at low energy.

Let us now look at the iron-μ-OH bridge interaction in detail. One of the oxygen p_z orbitals is involved in a s bond with H and the other oxygen p_z orbitals is involved in a σ bond with C and both are in the Fe_2O_2 plane. Since the two O ions are present as negative ions their $(p_x)^2$ and $(p_x)^2$ orbitals are filled. The O $(p_x)^2$ orbital is in the XZ plane and its partner $(p_y)^2$ orbital is perpendicular to the plane. The O p(σ) and p(π*) orbitals interact well with the Fe d_z2 and d_{xz} orbitals, respectively, this can be seen in the eight orbital maps at various energy levels depicted in Fig. 8. in which the in-phase and out-of-phase combinations of the non-bonding d-block orbitals can be seen. The 12 orbital maps at various energy levels depicted in Fig. 9. show the s and p orbitals involved in the σ-bonding of the OH and OC as well as the Fe–O bonds and the non-bonding p-block orbitals.

Upon reaction of $Fe_2(N)_6(O)_2$(μ-OL)(μ-OH) with molecular oxygen and the protons that remove water to form of intermediate P, the square active site opens up via a five ring $Fe_2(N)_6(O)_2$(μ-OL)(μ-η^1:η^1-O_2). The formation of intermediate Q $Fe_2(N)_6(O)_2$(μ-OL)(=O)$_2$ to give an open structure of two ferryl groups linked by a μ-oxo-C bridge of the ligand is consequently seen in Fig. 10. The complex of two $Fe(N)_3(O)$ fragments share three O ions, one from the μ-oxo-C back-bone of the ligand (OL) and two from a μ-η^1:η^1-O_2 bridge. The $Fe_2(N)_6(O)_2$ fragment has four non-bonding orbitals. The $Fe_2(N)_6(O)_2$(μ-OL) fragment has two non-bonding orbitals which react with di-oxygen to form the μ-η^1:η^1-O_2 bridge, since these non-bonding orbitals lie at low energy. We can now look at the bis-ferryl-hydroxy bridge interaction in detail. Two of the "t_{2g}" orbitals interact with the di-oxygen π_g^* orbitals. Since the π_g^* is lower in energy than the iron d orbitals, the resulting in-phase combination after interaction will have more oxygen π_g^* than metal d character and it will be occupied by electrons, at this stage two electrons are transferred from the metal "t2g" to di-oxygen to form O_2^{2-}. In this bound peroxo there is one O_2 orbital in the Fe_2O_2 plane, the anti-bonding σ_u^*, its partner π_g^*(p) is perpendicular to that plane. The oxygen $\pi_g^*(\sigma)$ and π_g^*(p) orbitals have good interactions with the iron d_{xy} and d_{xz} orbitals, respectively. In this bound peroxo form there is still one O_2 orbital bond, the bond order is thus one. In the next step in the catalytic cycles, cleavage of the peroxide O–O bond is supposed to occur, which results in the deformation of the planar active site. Yoshizawa et al. already suggested to change to O(equatorial)–Fe–O(peroxy) angles keeping other bond lengths and angles constant. By stretching the O–O bond the σ_u^* orbital falls in energy and the anti-bonding interactions are decreased. To cleave the dioxygen bond completely and form $Fe_2(N)_6(O)_2$(μ-OL)(=O)$_2$ it is necessary to fill the anti-bonding σ_u^* orbital by two electrons. The orbitals for the iron core in the O=Fe–O–Fe=O bis-ferryl (re)active site with a μ-oxo-L and a μ-hydroxo bridge are shown in Fig. 10. Since in $Fe_2(N)_6(O)_2$(μ-OL)(OCH_3)(OH) the two irons are in a nearly octahedral environment, there are six filled "t_{2g}" orbitals below the four empty "e_g" orbitals, this behaviour is characteristic for two iron atoms that interact weakly. The frontier orbitals have significant d-character, the four unpaired electrons can be counted for each of the two individual iron ions. For the intermediate Q the orbitals that participate at the active site as binding orbitals are seen, the Fe–O covalent σ-bond and the C–O σ-bond as well as the σ- and π-bonds of the ferryl Fe=O in the plane of the Fe–O–Fe bridge can be seen.

3.3. Oxidation catalysis

Study of the adamantane, cyclohexane and methane C–H oxidation permits to study CH bonds in primary, secondary or tertiary C atoms as shown in Table 10. The allylic oxidation of cyclohexene C–H bonds is also studied and the extent of double bond oxidation is compared for the different catalysts. The hydrogen peroxide, alkylperoxide and cyclohexylperoxide decomposition on these diiron complexes also reveals several interesting characteristics [38–50]. In the catalase reaction the hydrogen peroxide is decomposed giving water and oxygen. The $[Fe_2(HPTP)(\mu\text{-OH})]^{4+}$ complex demonstrates a higher catalase activity than the $[Fe_2(HPTB)(\mu\text{-OH})]^{4+}$ complex. The $[Fe_2(HPTB)(\mu\text{-OH})]^{4+}$ complex is generally more selective in oxidation reactions. In solution

Table 10
Alkane oxidation (product selectivities, %)

Adamantane (%)[a]	Conversion	Adamantan-1-ol	Adamantan-2-ol	Adamantan-2-one	Adamantan-1-ol-2-one	1 and 2-Cl-adamantane	Adamantan1-00tBu
HPTB/Fe	7.5	40.4	6.7	4.5	1.5	2.9	44.0
HPTB/Fe/HMS	5.1	26.5	6.6	3.7	0	8.2	55.0
HPTP/Fe	7.0	67.3	13.2	9.8	2.0	9.8	4.5
HPTP/Fe/HMS	4.6	34.0	11.6	8.1	0	56.4	0
Cyclohexane (%)[a]		*c*-Hexan-ol	*c*-Hexan-one	*c*-Hexan-OOH	*c*-Hexan-OOtBu		
HPTB/Fe	6.4	33.4	57.5	3.6	5.4		
HPTB/Fe/HMS	4.4	29.8	52.4	8.5	9.5		
HPTP/Fe	5.2	38.8	47.0	5.2	8.7		
HPTP/Fe/HMS	3.6	36.5	44.5	9.7	9.3		
Cyclohexene (%)[b]		*c*-Hexan-oxide	*c*-Hexan-1,2-diol	Adipoïne	*c*-Hexan-3-one	Epoxy *c*-hexen-3-one	
HPTB/Fe	15.4	81.9	2.3	1.6	3.9	8.3	
HPTB/Fe/HMS	13.5	82.1	0	5.4	5.6	0	
HPTP/Fe	25.0	88.9	1.4	1.4	5.6	2.5	
HPTP/Fe/HMS	18.1	88.5	0	5.9	5.7	0	
Methane (%)[c]		Methanol	Formaldehyde	Formic acid			
HPTB/Fe	1.2	82.9	4.9	12.2			
HPTB/Fe/HMS	0.8	74.5	8.8	16.7			
HPTP/Fe	1.4	65.3	13.5	21.2			
HPTP/Fe/HMS	1.1	56.8	19.7	23.5			

[a] Adamantane and cyclohexane oxidation (activity and selectivity, %) 0.05 g Fe/HPTP or Fe/HPTB catalyst (0.05 mmol), 0.2 g adamantane (1.5 mmol) or 0.2 g cyclohexane (2.4 mmol) and 1.8 g *t*butylhydroperoxide (*t*BHP, 16 mmol) in 4 g CH_2Cl_2, for 24 h at 293 K;

[b] Cyclohexene oxidation (activity and selectivity, %) 0.1 mmol Fe/HPTP or Fe/HPTB catalyst, 0.2 g cyclohexene (2.4 mmol) in 2 g CH_2Cl_2 and 1.8 g *t*butylhydroperoxide (*t*BHP, 16 mmol) for 24 h at 293 K;

[c] Methane oxidation (activity and select., %) 0.1 mmol Fe/HPTP/B catalyst, 2 g H_2O_2 (dilution of 30% soln. in H_2O, 18 mmol) is reacted with about 5 Torr of CH_4 equilibrated on the catalyst for 4 h at 293 K. Residual H_2O_2 is decomposed. Extraction of reaction mixture with diethylether is used for product isolation and GC and GC–MS analysis. Activity is determined based on hydrogen peroxide conversion and a conversion of 2–3 TO numbers is in accordance with $[(FeOCH_3)_2(HPTB)(\mu\text{-}OCH_3)]^{2+}$ adducts.

$[Fe_2(HPTP)(\mu\text{-}OH)]^{4+}$ also shows a higher extent of secondary oxidation of alcohols to consequent oxidation products, such behavior is not encountered for the enzyme as MMO. In the oxidation of adamantane by tBHP with $[Fe_2(HPTP)(\mu\text{-}OH)]^{4+}$ and $[Fe_2(HPTB)(\mu\text{-}OH)]^{4+}$ can abstract hydrogen from adamantane. $[Fe_2(HPTP)(\mu\text{-}OH)]^{4+}$ has a significantly higher selectivity for the secondary (25%) versus tertiary (75%) CH bonds, such behavior is reminiscent of this observed for MMO, where the selectivity for primary > secondary > tertiary C–H bonds has been observed. $[Fe_2(HPTB)(\mu\text{-}OH)]^{4+}$ has a lower selectivity for the secondary (12%) versus tertiary (88%) CH bonds. The decompostion of adamantyl-peroxydes ROOH with alkyl peroxyde radicals to form an adamantyl-tbutylperoxyde ROOR adduct and molecular oxygen at selectivities of 44–55% is observed on $[Fe_2(HPTB)(\mu\text{-}OH)]^{4+}$. The decompostion of adamantyl-tbutylperoxyde ROOR and adamantyl-peroxydes ROOH to form adamantanol ROH alcohols is observed on $[Fe_2(HPTP)(\mu\text{-}OH)]^{4+}$. Supported complexes and especially the $[Fe_2(HPTP)(\mu\text{-}OH)]^{4+}$ complexes react with the solvent and chlorinate adamantane preferentially in a secondary position (29% secondary/18% tertiary).

In the oxidation of cyclohexane by tBHP with $[Fe_2(HPTB)(\mu\text{-}OH)]^{4+}$ and $[Fe_2(HPTP)(\mu\text{-}OH)]^{4+}$ the formation of cyclohexanol and cyclohexanone is observed. Upon complex heterogenisation on HMS f.e. with $[Fe_2(HPTB)(\mu\text{-}OH)]^{4+}$-HMS the formation of 80–90% cyclohexanol and one and upto 10–20% of intermediate oxidation products such

as cyclohexyl-hydroperoxide and *tert*-butylperoxide are seen. These two alkylperoxide products are increasingly found in the oxidation with the supported complexes. A 1:1 and a 2:1 ratio of cyclohexanone to ol is obtained for $[Fe_2(HPTP)(\mu\text{-}OH)]^{4+}$ and $[Fe_2(HPTB)(\mu\text{-}OH)]^{4+}$, respectively. Cyclohexen-1-ol is the most important product formed for both the homogeneous and heterogeneous catalysts. Cyclohexyl-hydroperoxide is completely converted into cyclohexen-1-ol on the homogeneous catalysts and it is the most important intermediate or by-product (upto 10% of the selectivity) formed for the $[Fe_2(HPTB/P)(\mu\text{-}OH)]^{4+}$-HMS catalysts.

In the oxidation of the olefin cyclohexene by tBHP with $[Fe_2(HPTB)(\mu\text{-}OH)]^{4+}$ and $[Fe_2(HPTP)(\mu\text{-}OH)]^{4+}$ the epoxide is formed. Small amounts of its hydrolysis products such as diol and adipoïne are also seen. On $[Fe_2(HPTB/P)(\mu\text{-}OH)]^{4+}$-HMS epoxide is also formed but no diol is seen. With all catalysts in the presence of allylic hydrogens a low yield of ketone adducts is seen. $[Fe_2(HPTP/B)(\mu\text{-}OH)]^{4+}$ reveals an interplay of allylic oxidation to cyclohexen-3-ol and -3-one and epoxidation products. Epoxy-cyclohexen-3-one can be obtained by epoxidation with $[Fe_2(HPTP)(\mu\text{-}OH)]^{4+}$ of the deactivated cyclohexen-3-one. Cyclohexenyl-3-hydroperoxide may decompose on $[Fe_2(HPTB)(\mu\text{-}OH)]^{4+}$ to form epoxy-cyclohexen-3-one via a rearrangement. The latter is formed with higher selectivity compared to the initial epoxy-cyclohexene.

In the oxidation of methane on $[Fe_2(HPTB)(\mu\text{-}OH)]^{4+}$ by hydrogen peroxide the shunt pathway is again used to avoid working with oxygen and a reductant such as hydrogen or NADPH which is used by the enzyme. Using hydrogen peroxide as mono-oxygen donor the formation of methanol from methane is observed. $[Fe_2(HPTP)(\mu\text{-}OH)]^{4+}$ has a significantly higher selectivity for the primary versus secondary CH bonds, such behavior is reminiscent of this observed for MMO. Further oxidation products such as formaldehyde and formic acid are increasingly found in oxidation of methane by $[Fe_2(HPTP)(\mu\text{-}OH)]^{4+}$. The exchange of ^{18}O at the active site of these HPTP complexes was previously demonstrated [26] by the incorporation of the oxygen from $^{18}O_2$. $[Fe_2(HPTP)(\mu\text{-}OH)]^{4+}$ forms more secondary oxidation products compared to $[Fe_2(HPTB)(\mu\text{-}OH)]^{4+}$. With the methanol formed upto 3 methoxy groups can be coordinated on $[(FeOCH_3)_2(HPTB)(\mu\text{-}OCH_3)]^{2+}$.

3.4. Conclusions

Various groups have started immobilizing entire enzymes in mesoporous silicates [57–60]. We have previously shown that confinement of the active site is required in order to modify the behavior of the complex to mimic the MMO enzymatic activity [24–29], this can be achieved within the voids of HMS. Inorganic enzyme mimics lack the cooperativity seen in enzymes, so if the mimics come within the 5% of rate of the enzymatic catalysis such effects are marked [10]. Silica or alumino-silica lattices generally decrease life-times of radicals in solution, as the lattice wall generally decomposes them. In inorganic model systems the rate at which oxygen can be formed on precisely tailored active sites points to the catalase properties of the catalyst. The maximal rate of the formation of MMO type methane oxidation products requires that the competing reactions are minimized and the hydrogen peroxide is used efficiently [27]. For the reduction the MMO system uses a tyrosine electron donor shunt as this explains that after the oxidation in MMO most probably a tyrosine is involved in the reduction. Such a function may result from partial hydroxylation of phenylalanine 188 in the enzyme, to give a tyrosine radical [3,9,10].

Binuclear iron(III) complexes with an Fe–O–Fe bridge can activate molecular oxygen provided the Fe–Fe distances are short and are thus active models for MMO. The use of hydrogen peroxide in our experiments for the oxidation of methane allows us to use the shunt pathway, and avoids the more complex use of oxygen in combination with a co-reductant. The extent of dilution of the hydrogen peroxide is an issue when comparing our results with the data of Liu et al. [10] in which 1000-fold more diluted peroxide solutions are used when working with the enzyme components. This is necessary in order not to destroy the active site. The $[Fe_2(HPTB/P)(=O)_2]^{3+}$ complex is active in the hydroxylation of the adamantane, cyclohexane and methane C–H bonds of primary, secondary or tertiary C atoms and the epoxidation. The structure is activated in solution and the reactivity of $[Fe_2(HPTB/P)(=O)_2]^{3+}$ complexes is due to the two ferryl groups which are 0.2 Å closer for

HPTP compared to HPTB. The attack of the high energy CH bond is possible due to the electronic nature and the geometry of this active site. The reactivity of the slightly asymmetric $[Fe_2(HPTP)(\mu\text{-}O_2)]^{3+}$ complexes can originate from a side-on coordinated peroxo group. Upon interactions with peroxides the nature of the complexes may change since formally a transition from the OH^- to the O_2^{2-} species is expected to give a one electron change to proceed from a III, III to a III, IV and consequent bond braking by filling up the anti-bonding levels in the O–O bond a IV, IV state can be realized. The attack of an electron rich alkane leads to the peroxo adduct formation, in a sort an unwanted dioxygenase type side reaction. If at the active site the alkyl-peroxide is stabilized, the inter- or intra-molecular rearrangement are strongly disfavored. Allylic oxidation is more commonly observed with olefins and iron peroxides in absence of coordinating ligands. Time on stream data show that clay, HMS and MCM-41 supported complexes deactivate more slowly in catalysis than complexes in solution. This is also reflected in higher turnovers seen for the HMS and MCM-41 supported complexes.

The unique reactivity of the methane monoöxygenase (MMO) type intermediate $[Fe_2(=O)_2(HPTB/P)]^{3+}$ complexes with their two ferryl units present, is a result of the electronic and geometric coöperativity between two active sites of the cytochrome P-450-type, which makes them much more effective in the primary C–H bond activation.

Acknowledgements

PPKG thanks ESA and SSTC for financial support of PRODEX under contract ESA no. 15380/01/NL/SFe, thanks the FNRS FRFC Program for contract 2.453.02F1 and the Eu under COST Action D 21 for funding, the UCL FSR for a research grant, Guido Langouche from the K.U. Leuven, Belgium for the Mossbauer measurements, Francesco Faglioni from the MSC, Beckman Institute, CalTech, Pasadena, CA, USA for useful discussions.

References

[1] K. Yoshizawa, K. Ohta, T. Yamabe, R. Hoffmann, J. Am. Chem. Soc. 119 (1997) 12311.
[2] A.E. Shilov, G.B. Shulpin, Chem. Rev. 97 (1997) 2879.
[3] T. Lovell, J. Li, L. Noodleman, Inorg. Chem. 40 (2001) 5251.
[4] P.E. Siegbahn, R.H. Crabtree, J. Am. Chem. Soc. 119 (1997) 3103.
[5] R.H. Crabtree, Chem. Rev. 95 (1995) 987.
[6] D.M. Kurtz, Chem. Rev. 90 (1990) 585.
[7] S.J. Lippard, Angew. Chem. Int. Ed. Engl. 27 (1988) 344.
[8] D. Lee, S.J. Lippard, Inorg. Chem. 41 (2002) 827.
[9] A.C. Rosenzweig, C.A. Frederick, S.J. Lippard, P. Nordlund, Nature 366 (1993) 537.
[10] K.E. Liu, C.C. Johnson, M. Newcomb, S.J. Lippard, J. Am. Chem. Soc. 115 (1993) 939.
[11] K.E. Liu, D. Wang, B.H. Huynh, D.E. Edmonson, A. Salifoglou, S.J. Lippard, J. Am. Chem. Soc. 116 (1994) 7465.
[12] K.E. Liu, A.M. Valentine, D. Que, D.E. Edmonson, E.H. Appelman, T. Spiro, S.J. Lippard, J. Am. Chem. Soc. 117 (1995) 4997.
[13] L. Shu, J.C. Nesheim, K. Kauffmann, E. Munck, J.D. Lipscomb, L. Que Jr., Science 275 (1997) 515.
[14] L. Que, Y. Dong, Acc. Chem. Res. 29 (1996) 190.
[15] Y. Dong, S. Yan, V.G. Young Jr., L. Que Jr., Angew. Chem. 108 (1996) 674.
[16] R.E. Norman, R.C. Holz, S. Menage, L. Que, Jr., Zhang, J.H. O'Connor, Inorg. Chem. 29 (1990) 4629.
[17] S. Menage, B.A. Brennan, C. Juarez-Garcia, E. Munck, L. Que Jr., J. Am. Chem. Soc. 112 (1990) 6423.
[18] A.F. Shestakov, A.E. Shilov, J. Mol. Cat. A. 105 (1996) 1–7.
[19] A.K. Rappe, W.A. Goddard III, J. Phys. Chem. 95 (1991) 3358.
[20] A.K. Rappe, C.J. Casewit, K.S. Colwell, W.A. Goddard, W.M. Skiff, J. Am. Chem. Soc. 114 (1992) 10024.
[21] A. Van Duin, S. Dasgupta, F. Lorant, W.A. Goddard III, J. Phys. Chem. A. 105 (2001) 9396.
[22] S. Shaik, M. Filatov, D. Schröder, H. Schwarz, Chem. Eur. J. 4 (1998) 193–199.
[23] S. Dedysh, N.S. Panikov, W. Liesack, R. Grozkopf, J. Zhou, J.M. Tiedje, Science 282 (1998) 281.
[24] P.P. Knops-Gerrits, A. Weiss, S. Dick, P.A. Jacobs, Stud. Surf. Sci. Catal. 110 (1997) 1061.
[25] P.P. Knops-Gerrits, A.M. Van Bavel, G. Langouche, P.A. Jacobs, in: Derouane et al. (Eds.), Proceedings of NATO ASI, Vilamoura, Portugal, 25 May–6 June 1997, p. 215.
[26] P.P. Knops-Gerrits, A. Verberckmoes, R.A. Schoonheydt, M. Ichikawa, P.A. Jacobs, Microporous Mesoporous Mater. 21 (1998) 475.
[27] P.P. Knops-Gerrits, P.A. Jacobs, W.A. Goddard III, Stud. Surf. Sci. Catal. 130 (2000) 1187.
[28] P.P. Knops-Gerrits, W.J. Smith, Stud. Surf. Sci. Catal. 130 (2000) 3531.
[29] P.P. Knops-Gerrits, P.A. Jacobs, A. Fukuoka, M. Ichikawa, F. Faglioni, W.A. Goddard III, J. Mol. Cat. A. 166 (2001) 3–5.
[30] Niemantsverdriet, J.W., Spectroscopy in Catalysis, VCH, Weinheim, 1993.
[31] P. Gutlich, R. Link, A. Trautwein, Mossbauer spectroscopy and transition metal chemistry, in: M. Becke et al. (Eds.), Inorganic Chemistry Concepts, vol. 3, Springer, Berlin, 1978.
[32] G. Vanko, Z. Homonnay, S. Nagy, A. Vertes, H. Spiering, P. Gutlich, J. Chem. Phys. 108 (1998) 8472.

[33] E. Munck, Physical methods in bioinorganic chemistry, L. Que, Jr. (Ed.), University Science Books, Sausalito, CA, USA, 2000, p. 287.
[34] R.C. Reem, E.I. Solomon, J. Am. Chem. Soc. 109 (1987) 1216.
[35] T.E. Westre, P. Kennepohl, J.G. DeWitt, B. Hedman, K.O. Hodgson, E.I. Solomon, J. Am. Chem. Soc. 119 (1997) 6297.
[36] J.J. Girerd, Y. Journaux, Physical methods in bioinorganic chemistry, L. Que, Jr. (Ed.), University Science Books, Sausalito, CA, USA, 2000, p. 361.
[37] T.G. Spiro, R.S. Czernuszewicz, Physical methods in bioinorganic chemistry, L. Que, Jr. (Ed.), University Science Books, Sausalito, CA, USA, 2000, p. 59.
[38] G.S. Walker, J.A. Lapszewicz, G.A. Foulds, Catal. Today 21 (1994) 519.
[39] V.A. Durante, D.W. Walker, S.M. Gussow, J.E. Lyons, US Patent, 4,918,249, (1990).
[40] R.A. Sheldon, R. Van Santen, Catalytic Oxidation, World Scientific, Singapore, 1995.
[41] R.A. Sheldon, J.K. Kochi, Metal Catalysed Oxidations of Organic Compounds, Academic Press, New York, 1981.
[42] I. Arends, R.A. Sheldon, M. Wallau, U. Schuchart, Angew. Chem. Int. Ed. Engl. 36 (1997) 1144.
[43] D.H.R. Barton, J. Mol. Catal. 117 (1997) 3.
[44] M. Selke, M.F. Sisimore, R.Y.N. Ho, D.L. Wertz, J. Valentine, J. Mol. Catal. 117 (1997) 71.
[45] K.U. Ingold, J. Chem. Soc. (1961) 563.
[46] N. Kitajima, H. Fukui, Y. Moro-oka, Y. Mizutani, T. Kitagawa, J. Am. Chem. Soc. 112 (1990) 6402.
[47] P.P. Knops-Gerrits, D. De Vos, P.A. Jacobs, J. Mol. Catal. 117 (1997) 57.
[48] R.H. Fish, M.S. Konings, K.J. Oberhausen, R.H. Fong, W.M. Yu, G. Christou, J.B. Vincent, D.K. Coggin, R.M. Buchanan, J. Am. Chem. Soc. 110 (1991) 6898.
[49] R.H. Fish, K.J. Oberhausen, S. Chen, J.F. Richardson, W. Pierce, R.M. Buchanan, Catal. Lett. 110 (1993) 6898.
[50] J.B. Vincent, H.C. Huffman, G. Christou, Q. Li, M.A. Nanny, D.N. Hendrickson, R.H. Fong, R.H. Fish, J. Am. Chem. Soc. 110 (1988) 6898.
[51] J.S. Beck, J.C. Vartuli, W.J. Roth, M.E. Leonowicz, C.T. Kresge, K.D. Schmitt, C.T.W. Chu, D.H. Olson, E.W. Sheppard, S.B. McCullen, J.B. Higgins, J.L. Schlenker, J. Am. Chem. Soc. 114 (1992) 10834.
[52] P.T. Tanev, T.J. Pinnavaia, Science 267 (1995) 865.
[53] D. Zhao, J. Feng, Q. Huo, N. Melosh, G.H. Frederickson, B.F. Chmelka, G.D. Stucky, Science 279 (1998) 548.
[54] P. Yang, D. Zhao, D. Margolese, B.F. Chmelka, G.D. Stucky, Nature 396 (1998) 152.
[55] S. Inagaki, S. Guan, T. Ohsuna, O. Terasaki, Nature 416 (2002) 304.
[56] A. Corma, Chem. Rev. 97 (1997) 2373.
[57] J.F. Díaz, K.J. Balkus Jr., J. Mol. Catal. B: Enzym. 2 (1996) 115.
[58] L. Washmon-Kriel, V.L. Jimenez, K.J. Balkus Jr., J. Mol. Catal. B: Enzym. 10 (2000) 453.
[59] H.H.P. Yiu, P.A. Wright, N.P. Botting, J. Mol. Catal. B: Enzym. 15 (2001) 81.
[60] H. Takahashi, B. Li, T. Sasaki, C. Miyazaki, T. Kajino, S. Inagaki, Microporous Mesoporous Mater. 44–45 (2001) 755.